Aalto University

OPEN ACCESS

This is an electronic reprint of the original article.
This reprint may differ from the original in pagination and typographic detail.

Harnefors, Lennart; Hinkkanen, Marko; Riaz, Usama; Rahman, F. M. Mahafugur; Zhang, Lidong

Robust analytic design of power-synchronization control

Published in:
IEEE Transactions on Industrial Electronics

DOI:
10.1109/TIE.2018.2874584

Published: 29/03/2019

Document Version
Peer reviewed version

Please cite the original version:
Harnefors, L., Hinkkanen, M., Riaz, U., Rahman, F. M. M., & Zhang, L. (2019). Robust analytic design of power-synchronization control. *IEEE Transactions on Industrial Electronics*, *66*(8), 5810-5819. [8490668]. https://doi.org/10.1109/TIE.2018.2874584

This material is protected by copyright and other intellectual property rights, and duplication or sale of all or part of any of the repository collections is not permitted, except that material may be duplicated by you for your research use or educational purposes in electronic or print form. You must obtain permission for any other use. Electronic or print copies may not be offered, whether for sale or otherwise to anyone who is not an authorised user.

Robust Analytic Design of Power-Synchronization Control

Lennart Harnefors, *Fellow, IEEE*, Marko Hinkkanen, *Senior Member, IEEE*, Usama Riaz, F. M. Mahafugur Rahman, and Lidong Zhang, *Senior Member, IEEE*

***Abstract*—This paper addresses robust design of the active-power and dc-link control loops of power-synchronization control. Robustness is obtained by analytic gain selections which give large enough stability margins. The proposed design allows robust stability irrespective of the grid strength and of the operating point, the latter with one exception. The proposed design is compared to design based on the principle virtual synchronous machine. Experiments show that the time-domain results correlate well with the frequency-domain results.**

***Index Terms*—Grid-connected converters, robustness, stability analysis, voltage-source converters.**

I. Introduction

POWER-SYNCHRONIZATION CONTROL (PSC) of grid-connected voltage-source converters belongs to a family of control schemes where the dynamics of a synchronous machine are emulated. The principle is believed first to be suggested in [1], there called a virtual synchronous machine (VSM). The PSC variant first appeared in [2], [3], followed a year later by the synchronverter [4].

The three variants of synchronous-machine emulating control share the main features, fundamentally that the active power is controlled—as in a synchronous machine—by adjusting the converter-voltage angle [3]–[7]. A phase-locked loop (PLL) does not have to be used, at least not during normal operation [3], [6].

Yet, the objectives are different. Whereas the VSM and the synchronverter were conceived mainly for the purpose of grid forming—including the provision of a virtual inertia—PSC was conceived in order to enable a stable converter interconnection with a very weak grid. In such a situation, the standard principle of vector current control with outer loops is ineffective. This is because the active power is controlled by injecting a current component in phase with the point-of-common-coupling (PCC) voltage, whose angle is tracked by a PLL. This works well as long as the PCC voltage is reasonably stiff, but not when the grid is very weak and the PCC voltage varies to a great extent with the injected current [8].

The active-power control loop of PSC is often cascaded with an outer control loop for the dc-link voltage (or, equivalently, for the stored dc-link energy). Clearly, the selections of the active-power and dc-link control gains are critical for obtaining satisfactory performance in terms of bandwidth and stability margins. Even though since its conception, PSC has received significant attention in the scientific community [5], [9]–[13], design recommendations for the mentioned two gains are, to the best knowledge of the authors, so far missing. Selection is often made by trial and error. This is undesirable, since robustness of the closed-loop system is not guaranteed. Analytic gain selection whereby robustness is achieved is preferable, which is the main focus of the paper.

The contributions and outline of the paper are as follows. After setting the stage in Section II, in Section III the converter–grid interaction analysis for a purely inductive grid impedance made in [3] is revisited and slightly amended. The principal result thereof is an analytic selection recommendation for the active-power control gain, whereby adequate stability margins of the active-power control loop always are obtained. This gives a robust design, which allows the same controller tuning to be used, irrespective of the short-circuit ratio (SCR) of the grid and of the operating conditions. Both may vary, the former perhaps in an unknown way. For the recommended gain selection, a transfer function for the closed-loop system from the active-power reference to the obtained active power is derived. This allows the properties of the closed-loop system to be quantified, which is useful for the design of the dc-link control loop. Under the assumption that the integral action of the dc-link controller can be kept weak, a robust design of the dc-link control gain is made, also in Section III. Robust performance with adequate bandwidth is verified, except in certain cases of high reactive-current injection.

In Section IV, VSM design, where the active-power control gain is selected based on a specified frequency droop and where virtual inertia may be included, is revisited and compared to the proposed design.

Experimental results are presented in Section V.

II. System Model and PSC Principle

The traditional grid model consisting of an inductance L behind an infinite bus is adopted [3], see Fig. 1. The series resistance R is henceforth neglected. L is the sum of the filter

Manuscript received March 28, 2018; revised August 22, 2018; accepted September 13, 2018.

This work was supported in part by ABB, in part by the Finnish Foundation for Technology Promotion, and in part by the Walter Ahlström Foundation.

L. Harnefors and L. Zhang are with ABB, Corporate Research, 72178 Västerås, Sweden (e-mail: lennart.harnefors@se.abb.com; lidong.zhang@se.abb.com).

M. Hinkkanen, U. Riax, and F. M. Mahafugur Rahman are with the School of Electrical Engineering, Aalto University, 02150 Espoo, Finland (e-mail: marko.hinkkanen@aalto.fi; usama.riaz@aalto.fi; f.rahman@aalto.fi).

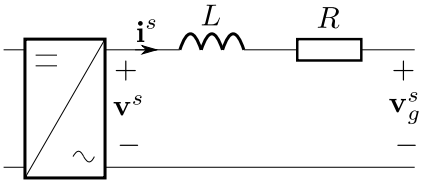

Fig. 1. Circuit model of a grid-connected voltage-source converter.

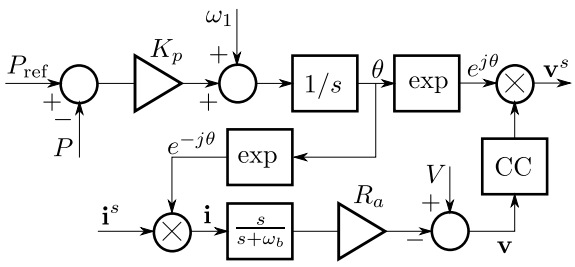

Fig. 2. Block diagram of PSC.

inductance of the converter, the inductance of the transformer which interfaces the converter to the grid (if such is used), and the grid inductance. The circuit model shown in Fig. 1 is obtained, where $\mathbf{v}^s$ and $\mathbf{v}_g^s$ respectively are the space vectors for the converter voltage and the grid voltage, whereas $\mathbf{i}^s$ is the space vector for the converter output current. The superscript ^{s} denotes that the space vector is expressed in the stationary ($\alpha\beta$) frame, i.e., it rotates with the angular synchronous frequency ω_1. The corresponding dq-frame space vector is denoted without a superscript, e.g., $\mathbf{i}$.

The grid voltage is considered stiff, i.e., its magnitude V_g is constant and the space vector rotates with the synchronous frequency. Fig. 1 gives

$$\mathbf{v}^s - sL\mathbf{i}^s = \mathbf{v}_g^s = V_g e^{j\omega_1 t} \tag{1}$$

where $s = d/dt$. To avoid having to split L into the grid and converter inductances, the SCR is here defined as seen from the converter terminals. This gives a lower value than the SCR seen from the PCC, but has otherwise no impact on the results. With this definition, the SCR is the inverse per-unit (p.u.) value of L

$$\text{SCR} = \frac{1}{L\ [\text{p.u.}]}. \tag{2}$$

The fundamental principle of PSC is to select the converter voltage as

$$\mathbf{v}^s = Ve^{j\theta} \tag{3}$$

where V is the converter-voltage magnitude. V may be varied in a closed control loop for the PCC voltage or the reactive power [3], [14]. However, for space constraints it is assumed that this control loop—if used—is slow enough to be disregarded, allowing V to be considered constant. Angle θ is governed by the control law

$$\frac{d\theta}{dt} = \omega_1 + K_p(P_{\text{ref}} - P) \tag{4}$$

where K_p is the active-power control gain, P is the active output power of the converter

$$P = \kappa\text{Re}\{\mathbf{v}^s(\mathbf{i}^s)^*\} = \kappa\text{Re}\{\mathbf{v}\mathbf{i}^*\}, \qquad \kappa = \frac{3}{2K^2} \tag{5}$$

and P_{ref} is the active-power reference. In (5), K is the space-vector scaling constant. For p.u. normalization of the quantities or power-invariant vector scaling ($K = \sqrt{3/2}$), $\kappa = 1$.

Remark: Throughout the paper, ω_1 is considered to be the *nominal* angular synchronous frequency. Particularly during grid disturbances, the local instantaneous angular grid frequency $\omega_g = d\theta/dt$ may differ from ω_1. Then, from (4)

$$P = P_{\text{ref}} + \frac{1}{K_p}(\omega_1 - \omega_g). \tag{6}$$

That is, PSC inherently adds a frequency droop, with droop gain $1/K_p$, to the active-power reference [16].

Equation (3) shall not be implemented as it stands, because a poorly damped closed-loop system would result. The remedy is to subtract a term with gain R_a—the so-called active resistance—from the converter voltage [3]. The term consists of a high-pass filtering of the synchronous (dq)-frame current vector $\mathbf{i} = e^{-j\theta}\mathbf{i}^s$

$$\mathbf{v} = V - H_a(s)\mathbf{i}, \qquad H_a(s) = R_a\frac{s}{s+\omega_b}. \tag{7}$$

The filter bandwidth ω_b shall be selected smaller than ω_1, typically in the range $0.1\omega_1$—$0.2\omega_1$, i.e., 0.1—0.2 p.u. [9], [12]. Vector $\mathbf{v}$ is then $\alpha\beta$ transformed as $\mathbf{v}^s = e^{j\theta}\mathbf{v}$, still with θ given by (4). Vector $\mathbf{v}^s$ serves as reference to the pulsewidth modulator, whose impact (time delay and added harmonics) here is disregarded. Fig. 2 shows the resulting block diagram. In addition to the algorithm described above, the block diagram includes an embedded current controller (CC). It is transparent during normal operation but acts to limit the current during transients when needed [2], [3]. This is particularly important for fault ride-through [15]. The CC is not impacted by the robust design proposed in this paper and is therefore not considered further.

III. Analysis and Robust Design

Based on analysis of the dynamics obtained by PSC, a robust design of the active-power control loop is made in this section, followed by a robust design of the dc-link control loop.

A. Open-Loop Dynamics

In [3], the response ΔP in the active power to an angular perturbation $\Delta\theta$ is derived, i.e., the open-loop response. In Appendix I, a variant of this derivation is presented. Unlike [3], the effect of the active resistance is accounted for from the beginning, whereas R is neglected. This gives a different numerator of the open-loop transfer function $G_{\theta P}(s)$ from $\Delta\theta$ to ΔP than that derived in [3]. Another difference is that the numerator coefficients—which are operating-point dependent—are here expressed in the components of the steady-state dq-frame converter current $\mathbf{i}_0 = i_{d0} + ji_{q0}$. As the steady-state complex output power at the converter terminals is given by

$$\kappa\mathbf{v}_0\mathbf{i}_0^* = \kappa V(i_{d0} - ji_{q0}) \tag{8}$$

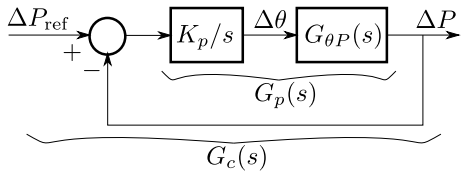

Fig. 3. Linearized closed-loop system.

it follows that i_{d0} and $-i_{q0}$ respectively are proportional to the active and reactive output powers. Hence, $i_{q0} < 0$ and $i_{q0} > 0$ respectively correspond to injection and absorption of reactive current. From Appendix I, the following transfer function is obtained:

$$G_{\theta P}(s) = \frac{\kappa V^2}{\omega_1 L} \frac{as^2 + [1 + a + b(s)]\omega_1^2}{s^2 + \frac{2H_a(s)}{L}s + \omega_1^2 + [\frac{H_a(s)}{L}]^2} \tag{9}$$

where

$$a = \frac{\omega_1 L i_{q0}}{V} \qquad b(s) = -\frac{H_a^2(s)}{V}\left(\frac{i_{q0}}{\omega_1 L} + \frac{|\mathbf{i}_0|^2}{V}\right). \tag{10}$$

The following observations can be made.

- A marginally stable system is obtained for $R_a = 0 \Rightarrow H_a(s) = 0$. (Since, in practice, $0 < R \ll R_a$, asymptotic stability is yet obtained, but with very poor damping [3].)
- As $\omega_b \to 0$, the high-pass filter reduces to the pure active resistance, i.e., $H_a(s) \to R_a$. Consequently, (9) reduces to a second-order system. The poles of (9) are then located at $s = -R_a/L \pm j\omega_1$, i.e., the damping increases with the SCR.
- The static gain $G_{\theta P}(0)$ is proportional to $1 + a + b(0)$ and is, thus, operating-point dependent. High injection of reactive current, giving $a < 0$, reduces the gain. This, in turn, reduces the bandwidth of the closed-loop system, see Section III-B.
- Equation (10) shows that the static gain is affected by the active resistance as well, via $b(s)$.
- For reactive-current injection, there is a right-half-plane zero, giving nonminimum-phase behavior. This too has a limiting effect on the closed-loop bandwidth [3].

B. Closed-Loop Dynamics

The active-power control law (4) can be expressed in perturbation variables as

$$\Delta\theta = \frac{K_p}{s}(\Delta P_{\rm ref} - \Delta P). \tag{11}$$

Equations (38) (in Appendix I) and (11) together form the closed-loop system shown in Fig. 3, whose open-loop and closed-loop transfer functions respectively are given by

$$G_p(s) = \frac{K_p G_{\theta P}(s)}{s} \qquad G_c(s) = \frac{G_p(s)}{1 + G_p(s)}. \tag{12}$$

1) Gain Selection for Robust Stability: The stability of $G_c(s)$ can be analyzed by applying the Nyquist criterion to $G_p(s)$. For robustness, the phase and gain margins ϕ_m and g_m need to be sufficiently large; an established recommendation is $\phi_m \geq 45^\circ$ and $g_m \geq 2$ [17]. On the other hand, too large stability margins may impair the bandwidth of the closed-loop system. A design which aims at the minimum recommended gain margin as therefore sought. This is formulated as the following theorem.

Theorem 1: Selecting

$$K_p = \frac{\omega_1 R_a}{\kappa V^2} \tag{13}$$

gives $g_m \geq 2$ of $G_p(s)$ for a negligible ω_b [implying $H_a(s) = R_a$], irrespective of the operating point (V, i_{d0}, i_{q0}) and the SCR.

Proof: See Appendix II.

The following may be noted concerning the recommended gain selection.

- Since the desired gain margin is always obtained and (13) is free of L, i.e., knowledge of the SCR is not needed, the design gives robust stability provided that the phase margin is sufficient. That so is the case is exemplified later.
- K_p is selected inversely proportional to V^2 and should be gain scheduled with any variations in V. During normal operation, this has a marginal effect, as V is kept at or near the nominal voltage (1 p.u.). On the other hand, it is important during fault-ride-through situations, when V temporarily may need to be reduced to a value much lower than the nominal, in order to avoid overcurrent. Keeping K_p at its nominal value during such situations may give insufficient gain.

2) Closed-Loop Transfer Function: Applying (13), interesting observations of the closed-loop transfer function can be made. Again, assuming a negligible ω_b—giving $H_a(s) = R_a$ and making b independent of s—the following transfer function is obtained:

$$G_c(s) = \frac{\frac{R_a}{L}[as^2 + (1 + a + b)\omega_1^2]}{s^3 + \frac{(2+a)R_a}{L}s^2 + [\omega_1^2 + (\frac{R_a}{L})^2]s + \frac{(1+a+b)\omega_1^2 R_a}{L}}. \tag{14}$$

An approximate factorization of the denominator is available

$$G_c(s) \approx \frac{\frac{R_a}{L}[as^2 + (1 + a + b)\omega_1^2]}{[s + \frac{(1+a+b)R_a}{L}][s^2 + \frac{(1-b)R_a}{L}s + \omega_1^2]}. \tag{15}$$

Expanding the denominator polynomial of (15), all coefficients except that for s match those of (14). The mismatch of the coefficient for s is negligible for $|a| \ll 1$ and $|b| \ll 1$.

The following observations of (15) can be made.

- There is a pole pair, whose relative damping increases with the SCR, as

$$\zeta = \frac{(1 - b)R_a}{2\omega_1 L}. \tag{16}$$

- There is a real pole, at $s = -(1 + a + b)R_a/L$, which dominates for a weak grid with $R_a/L < \omega_1$. The minimum bandwidth of $G_c(s)$ for low converter current (a and b small) is thus

$$\omega_{c,\min} \approx \frac{R_a}{L_{\max}} \tag{17}$$

where $L_{\max}$ is the maximum expected grid inductance ($L_{\max} = 1$ p.u. if SCR ≥ 1).

- For a strong grid with $R_a/L > \omega_1$, the pole pair dominates. If $\zeta < 1$, the pole pair is complex and the distance from each pole to the origin is ω_1; consequently, the maximum obtainable bandwidth of $G_c(s)$ is

$$\omega_{c,\max} \approx \omega_1. \tag{18}$$

  This explains why PSC has been found to be inferior to vector current control for strong grids: the bandwidth of the closed-loop system is inherently limited.
- Too large R_a may give a significant bandwidth reduction for weak as well as for strong grids. Suppose, for example, that $R_a = 1$ p.u., $i_{q0} = 0$, and $V = 1$ p.u. Then it follows from (10) that $b \to -1$ as $|i_{d0}| \to 1$ p.u., i.e., the real pole approaches the origin and the bandwidth approaches zero. As a compromise between low impact on the bandwidth and good enough damping of the pole pair, it is suggested to select

$$R_a = 0.2 \text{ p.u.} \tag{19}$$

  Then b may be neglected and the relative damping as given by (16) can be expressed as

$$\zeta = 0.1\,\mathrm{SCR}. \tag{20}$$

- High reactive-current injection ($i_{q0} < 0$) may significantly limit the bandwidth, to

$$\omega_{c,\mathrm{rci}} \approx (1+a)\frac{R_a}{L} = \left(1 + \frac{\omega_1 L i_{q0}}{V}\right)\frac{R_a}{L}. \tag{21}$$

  This is a risk particularly in fault-ride-through situations, where grid codes often require reactive-current injection, see [18] and the publications cited therein. The risk is present for weak grids (L large) as well as for strong grids (when V may need to be reduced to avoid overcurrent). Since the lower limit for a is -1, see Appendix III, $\omega_{c,\mathrm{rci}}$ approaches zero in the worst of situations [but then, on the other hand, the accuracy of the factorization in (15) deteriorates, as no longer $|a| \ll 1$]. Nevertheless, bandwidth reduction of $G_c(s)$ for high reactive-current injection needs to be accounted for if the PSC is cascaded with a dc-link controller, which is considered next.

C. DC-Link Control Loop

DC-link control can be added as an outer loop in cascade with the active-power control loop. If the converter losses are neglected, the dc-link dynamics can be expressed in the energy W_d stored in the dc link as

$$\frac{dW_d}{dt} = P_d - P \tag{22}$$

where P_d is dc-source power. The dc-link energy is related to the dc-link voltage v_d and the dc-link capacitance C_d as $W_d = (C_d/2)v_d^2$. Often, P_d is known and can be fed forward, possibly low-pass filtered (P_d^f), in the dc-link control law

$$P_{\mathrm{ref}} = F_d(s)(W_d - W_d^{\mathrm{ref}}) + P_d^f \tag{23}$$

where W_d^{ref} is the reference energy and $F_d(s)$ dc-link controller transfer function. With feedforward, the dc-link controller can be given weak integral action, allowing $F_d(s)$ to be approximated as a proportional controller $F_d(s) = K_d$. Gain K_d has the dimension angular frequency; it can be considered as the ideal dc-link control-loop bandwidth.

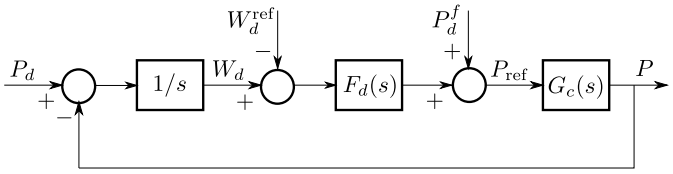

Fig. 4. DC-link control loop.

Together with the active-power control loop, (22) and (23) form the closed-loop system shown in Fig. 4, whose open-loop transfer function is $G_d(s) = K_d G_c(s)/s$. Robust design of the dc-link control gain can be made in a similar fashion as of the active-power control gain. To allow for a large enough phase margin (as exemplified below), a minimum gain margin of 4 is this time aimed at.

Theorem 2: Selecting

$$K_d \le \frac{\omega_1}{4}\sqrt{\frac{1-b}{2+a}} \tag{24}$$

gives $g_m \ge 4$ of $G_d(s)$ for a negligible ω_b.

Proof: See Appendix IV.

Due to selection recommendation (19) of R_a, b can be neglected in (24). Yet, because of the factor $1/\sqrt{2+a} = 1/\sqrt{2+\omega_1 L i_{q0}/V}$, (24) requires knowledge of L, i.e., of the SCR. However, this is an issue only for high reactive current, as otherwise a can be neglected. Furthermore, if restriction is made to (high) reactive-current injection,[1] i.e., $-1 \le a < 0$ (where the lower limit -1 is established in Appendix III), then (24) is fulfilled by the selection recommendation

$$K_d = \frac{\omega_1}{4\sqrt{2}} \approx 0.18\omega_1. \tag{25}$$

Recommendation (25) for a 50-Hz grid gives an ideal bandwidth of $K_d = 56$ rad/s, which should be sufficient in many cases.

Example 1: Fig. 5 shows Nyquist diagrams for the active-power and dc-link control loops, all for $V = \omega_1 = 1$ p.u., $\kappa = 1$, $\omega_b = 0.1$ p.u., and the recommended parameter selections (13), (19), and (25) [(12)—not the special case (14)—is used for $G_c(s)$ in $G_d(s) = K_d G_c(s)/s$]. Two operating conditions are considered, both for full current ($|\mathbf{i}_0| = 1$ p.u.): high active-current injection (upper subplots) and high reactive-current injection (lower subplots). The latter condition is characteristic for a fault situation, when the grid voltage is depressed and reactive current is injected to keep the converter voltage up. Three values of L are considered, corresponding respectively to $\mathrm{SCR} = 10$, $\mathrm{SCR} = 3$, and $\mathrm{SCR} = 1$, i.e., a strong, a fairly weak, and a very weak grid.

For $G_p(s)$ it can be observed that $g_m > 2$ in all cases, even though $\omega_b > 0$, contrary to the restriction in Theorem 1. Interestingly, the smallest phase margin is obtained for $\mathrm{SCR} = 10$.

[1] This restriction is relevant, as high reactive-current injection, e.g., for grid-code compliance, is more common a scenario than high reactive-current absorption [18].

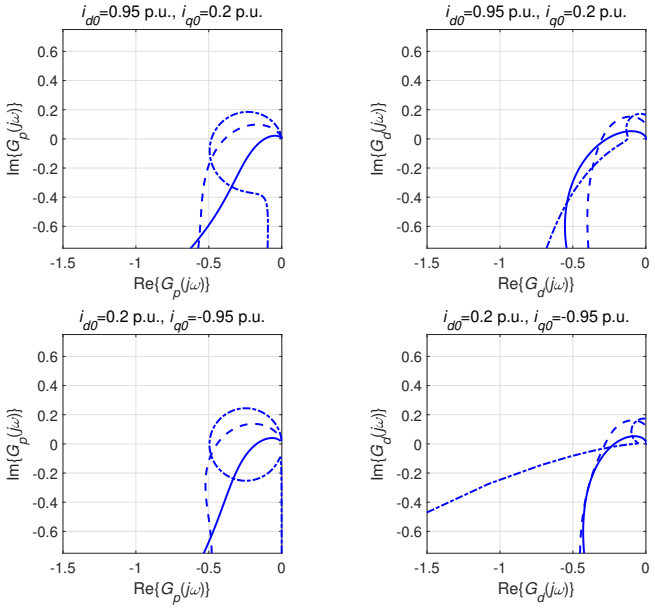

Fig. 5. Nyquist diagrams for (solid) $\mathrm{SCR} = 10$, (dashed) $\mathrm{SCR} = 3$, and (dashed-dotted) $\mathrm{SCR} = 1$.

For $G_d(s)$ some curves show slightly smaller gain margin than the desired minimum 4, because $\omega_b > 0$, contrary to the restriction in Theorem 2. Yet, sufficient stability margins are obtained in all cases but for the very-weak-grid case with high reactive-current injection. Low phase margin in this case is a result of the reduced bandwidth of $G_c(s)$ according to (21). A similar reduction of the phase margin is obtained with high reactive-current injection for a stronger grid and a depressed voltage magnitude (V significant smaller than 1 p.u.).

IV. VSM Design

The objective of the VSM is to provide grid forming by means of frequency droop and virtual inertia. The former is inherent in PSC, see (6), whereas the latter can be introduced by adding a low-pass filter to the PSC control law [2], [16]. The purpose of this section is to compare the robust design proposed in Section III to typical VSM designs.

For a VSM, the dc-source power P_d has to be controllable to allow the active output power P to respond to grid-frequency variations. This requires either dc-side energy storage [19], [20] or a dc-side power source with headroom for increased output [21]. For VSM design it is therefore preferable to perform dc-link control via P_d rather than in cascade with the active-power control loop (the latter would, in fact, counteract the grid-forming property).

Virtual inertia can be added by emulating the swing equation of a synchronous machine

$$M\frac{d\omega_g}{dt} = P_g - P - K_D(\omega_g - \omega_f) \qquad \frac{d\theta}{dt} = \omega_g \quad (26)$$

where M is the ω_1-scaled virtual inertia, ω_g is the virtual machine speed (which, since θ is formed by integrating ω_g, also is the local angular grid frequency), P_g is the virtual governor power, K_D is the virtual mechanical damping constant, and

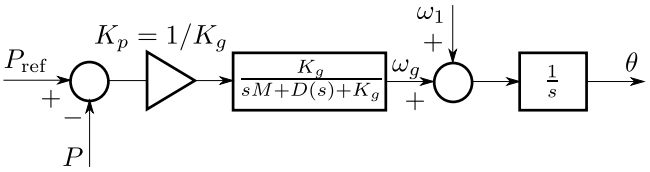

Fig. 6. PSC with an added low-pass filter for virtual inertia and damping.

ω_f is a low-pass filtering of ω_g through $\alpha_f/(s+\alpha_f)$ [22]. Thus, (26) can be equivalently expressed as

$$[sM + D(s)]\omega_g = P_g - P \qquad \theta = \frac{1}{s}\omega_g \quad (27)$$

where $D(s) = K_D s/(s+\alpha_f)$. M can be expressed in the inertia constant H (with dimension time) and in the rated apparent power of the converter S_{base} as [23], [24]

$$M = \frac{2S_{\mathrm{base}}H}{\omega_1}. \quad (28)$$

Unlike the governor of a synchronous machine, P_g can be adjusted without lag and is set by adding a frequency droop to the active-power reference [16], [22]

$$P_g = P_{\mathrm{ref}} + K_g(\omega_1 - \omega_g), \qquad K_g = \frac{S_{\mathrm{base}}}{\sigma\omega_1} \quad (29)$$

where σ is the droop in percentage of the VSM power rating.

Combining (27) and (29), the feedback loop formed by the frequency droop can be resolved in a low-pass filter with unity static gain

$$\theta = \frac{1}{s}\frac{K_g}{sM + D(s) + K_g}\left[\omega_1 + \frac{1}{K_g}(P_{\mathrm{ref}} - P)\right]. \quad (30)$$

(For $K_D = 0 \Rightarrow D(s) = 0$, a first-order low-pass filter with time constant $M/K_g = 2\sigma H$ is obtained.) Since ω_1 is the nominal angular synchronous frequency and thus is constant, the entry point of ω_1 can be relocated to the output of the low-pass filter, as shown in Fig. 6. The frequency droop (29) gives the gain selection [which can also be obtained by comparing (6) and (29)]

$$K_p = \frac{1}{K_g} = \frac{\sigma\omega_1}{S_{\mathrm{base}}}. \quad (31)$$

If the droop is selected similar to that of the synchronous machines in the grid, typically $\sigma = 0.04$—0.05, the VSM gives a corresponding contribution to the primary frequency control. With $V = \omega_1 = 1$ p.u., the proposed design (13), with (19), gives $K_p = 0.2$ p.u. VSM design (31), on the other hand, gives $K_p = \sigma$ [p.u.] for $S_{\mathrm{base}} = 1$ p.u., i.e., typically a much smaller gain. The implications thereof are studied in the following two examples.

Example 2: VSM design with $H = 0$ (called VSM0H [25]), $K_D = 0$, and $\sigma = 0.05$ is compared to the proposed design. For completeness also cascaded dc-link control is studied, even though this is not recommended for VSM design. Fig. 7 shows Nyquist diagrams for the active-power and dc-link control loops, both for $V = \omega_1 = S_{\mathrm{base}} = 1$ p.u., $\kappa = 1$, and the recommended parameter selections (19) and (25). A relatively weak grid ($\mathrm{SCR} = 2$) and relatively high active- and reactive-current injection ($i_{d0} = -i_{q0} = 0.7$ p.u.) are considered. The following can be observed.

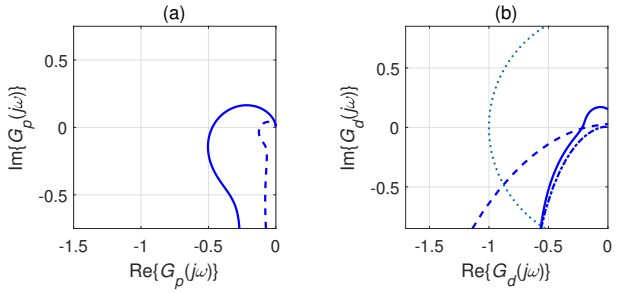

Fig. 7. Nyquist curves for (solid) the proposed design (13) and (dashed) VSM design (31), in both cases with K_d selected as (25). The dashed-dotted curve shows VSM design with K_d selected as 30% of (25).

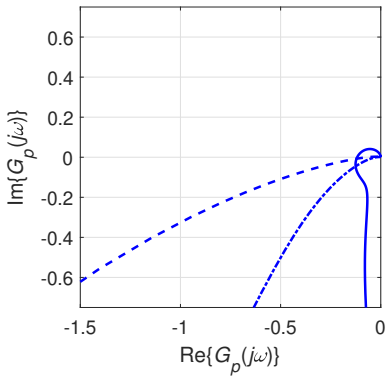

Fig. 8. Nyquist curves for VSM design with (solid) $H = K_D = 0$, (dashed) $H = 5$ s and $K_D = 0$, and (dashed-dotted) $H = 5$ s, $K_D = 50$ p.u., and $\alpha_f = 1$ rad/s.

- Because of a much smaller K_p, VSM design gives larger stability margins of $G_p(s)$ than the proposed design, i.e., further improved robustness of the active-power control loop. This may explain why an active resistance is absent in the synchronverter [4].
- The smaller K_p of VSM design is paid for by reduced robustness of $G_d(s)$ in the form of a fairly small phase margin. To obtain a similar phase margin as with the proposed design, K_d needs to be reduced to 30% of (25), see the dashed-dotted curve in Fig. 7(b). Consequently, the dc-link capacitance has to be 3.3 times larger than for the proposed design if similar dc-link-voltage fluctuations during transients and disturbances are to be obtained. This clearly shows that, with VSM design, it is preferable to control the dc link via the dc-source power.

Example 3: A virtual inertia $H = 5$ s (for a synchronous frequency of 50 Hz) is now included in the control law (30), still with $\sigma = 0.05$. This significantly reduces the phase margin of $G_p(s)$ as compared to $H = 0$, as demonstrated by the solid and dashed curves in Fig. 8. As shown by the dashed-dotted curve, the phase margin can be increased by introducing virtual mechanical damping. Cascaded dc-link control is effectively impossible with H in the range of seconds. The lag incurred from the low-pass filter in (30) would require K_d to be much smaller than (25), for the dc-link control loop to be stable.

TABLE I
TEST-SYSTEM DATA

Variable/parameter	Actual value	Normalized value
Rated power	12.7 kVA	1 p.u.
Rated voltage	$\sqrt{2/3} \cdot 400$ V	1 p.u.
Rated current	$\sqrt{2} \cdot 18.3$ A	1 p.u.
Base impedance	12.6 Ω	1 p.u.
Nominal grid frequency	50 Hz	1 p.u.
DC-link voltage v_d	650 V	2 p.u.
DC-link capacitance C_d	2.1 mF	8.3 p.u.
Sampling frequency	8 kHz	160 p.u.
Switching frequency	4 kHz	80 p.u.
Active resistance R_a	4.4 Ω	0.2 p.u.
Filter bandwidth ω_b	31 rad/s	0.1 p.u.
DC-link control gain K_d	56 rad/s	0.18 p.u.

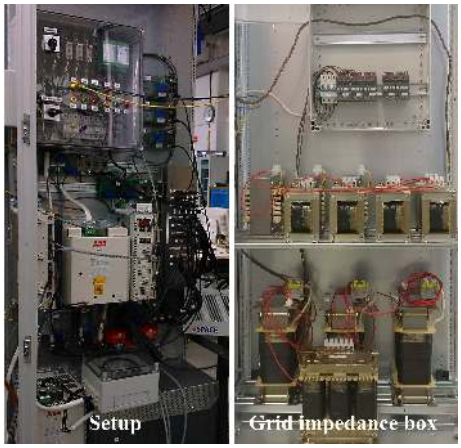

Fig. 9. Photo of the experimental setup.

V. EXPERIMENTAL RESULTS

The proposed robust PSC design is here verified experimentally on a back-to-back (grid and dc-source) two-level converter system, which is illustrated in Figs. 9 and 10 and whose data are given in Table I. The converter is controlled by a dSPACE DS1006 processor board. Forward-difference discretization of the continuous-time transfer functions is used. Peak-value space-vector scaling (i.e., $K = 1$) is used. The active-power control loop uses gain selection (13).

A. Active-Power Control Only

$P_{\rm ref}$ is here set manually; the dc-link voltage is controlled by the dc-source converter. Figs. 11, 12, and 13 show results for four successive steps in $P_{\rm ref}$, respectively for three SCRs, i.e., very weak, semi-weak, and strong grids. The following observations can be made.

- Adequate performance is verified for all three SCRs, showing that the design is robust.
- For SCR $= 1$—owing to the (complex-conjugated) pole pair in (15)—there is slight ringing in the step-response transients. However, there is no overshoot, since the real pole in (15) dominates the step response.
- For SCR $= 3$, the real pole in (15) is located further from the origin, so the rise time is shorter. Improved damping

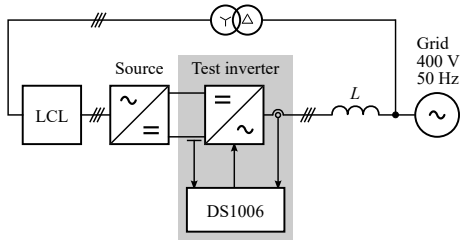

Fig. 10. Schematic of the experimental setup.

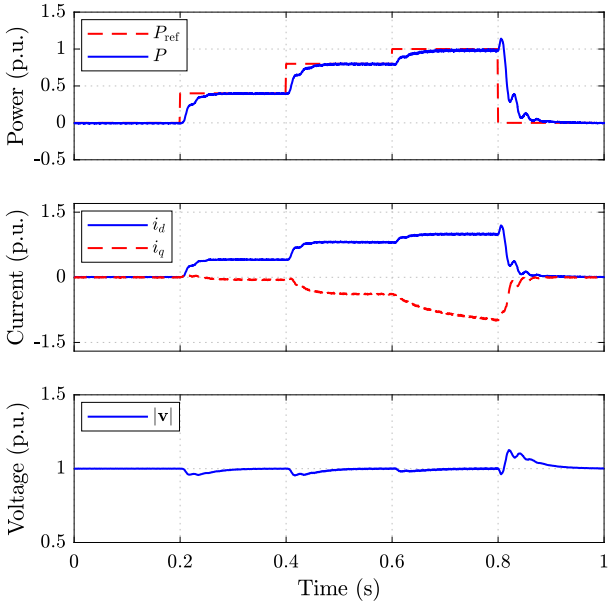

Fig. 11. Active-power control only for $\mathrm{SCR} = 1$.

of the pole pair in (15) reduces the ringing to a small overshoot.

- For $\mathrm{SCR} = 10$, yet slightly shorter rise time is obtained, but because of the reduced phase margin of $G_p(s)$—see Fig. 5—larger overshoot is obtained.

In addition, Fig. 14 illustrates the effect of transients in the grid frequency. In adherence with (6), for $K_p = 0.2$ p.u. there is a 0.1-p.u. power increase for a 0.02-p.u. frequency drop.

B. Cascaded DC-Link and Active-Power Control

Here, steps of ± 0.2 p.u. about the nominal dc-link-voltage reference 2 p.u. are made, again for three SCRs, see Figs. 15, 16, and 17. The best performance in terms of short rise time and small overshoot (ringing) of the dc-link voltage is obtained for $\mathrm{SCR} = 3$. This is consistent with the Nyquist curves of $G_d(s)$ for $i_{d0} = 0.95$ p.u. (although here $i_{d0} = 0.6$ p.u.) shown in Fig. 5. The curve for $\mathrm{SCR} = 3$ has the lowest sensitivity peak, i.e., the largest minimum distance to -1. Yet, all three cases show satisfactory performance, verifying the robustness of (25).

VI. Conclusion

Robust design recommendations for the active-power and dc-link control gains of PSC were presented. Although the

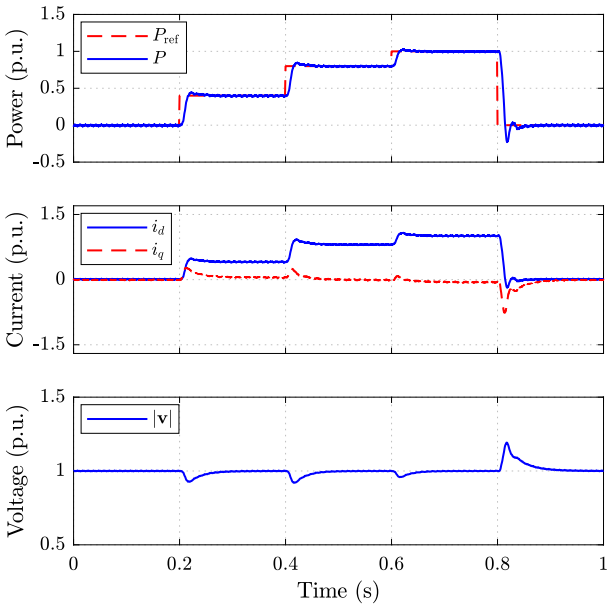

Fig. 12. Active-power control only for $\mathrm{SCR} = 3$.

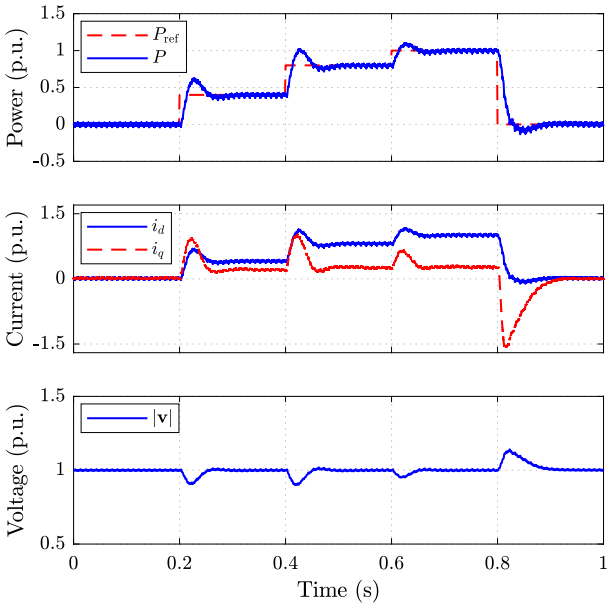

Fig. 13. Active-power control only for $\mathrm{SCR} = 10$.

derivations rely on some simplifying assumptions, robust performance irrespective of the SCR and of the operating point (with the possible exception of very high reactive-current injection) was verified experimentally. The proposed design was compared to VSM design, showing that for zero virtual inertia (VSM0H), even better robustness of the active-power control loop is typically obtained than for the proposed design. With virtual inertia, adding virtual mechanical damping is recommended in order to obtain an adequate phase margin. With VSM design, cascaded dc-link control is not recommended or is impossible. The proposed design recommendation for the active-power control gain is thus particularly suitable for cascaded dc-link control.

A suitable topic for further research is to study the impact

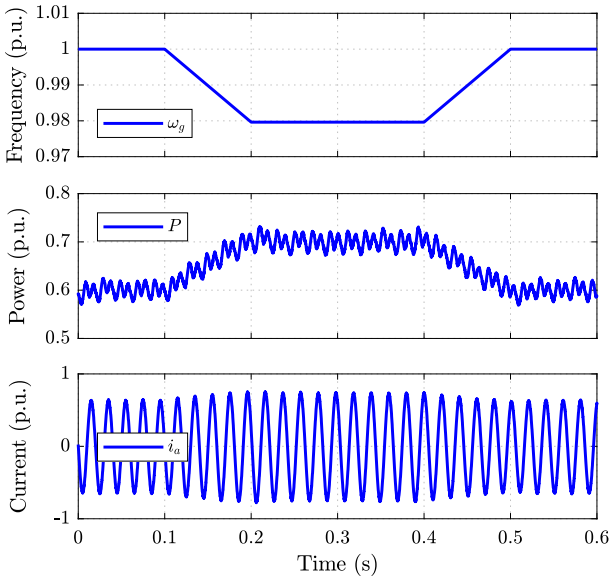

Fig. 14. Active-power control only for $\mathrm{SCR} = 10$, respose to grid-frequency transients in the active power and the phase-a current.

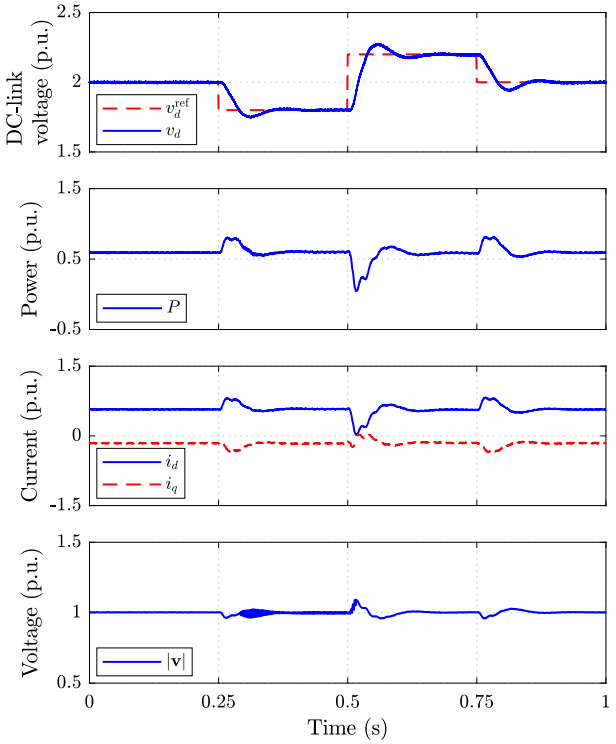

Fig. 15. Cascaded dc-link and active-power control for $\mathrm{SCR} = 1$.

of fast-acting PCC-voltage or reactive-power control together with the proposed design. As shown in [14], the active- and reactive-power control loops may have a nonnegligible interaction.

Appendix I

Unlike in [3], complex transfer functions are here used, thereby obtaining simpler expressions. To facilitate linearization of (3) and (5), θ is expressed as

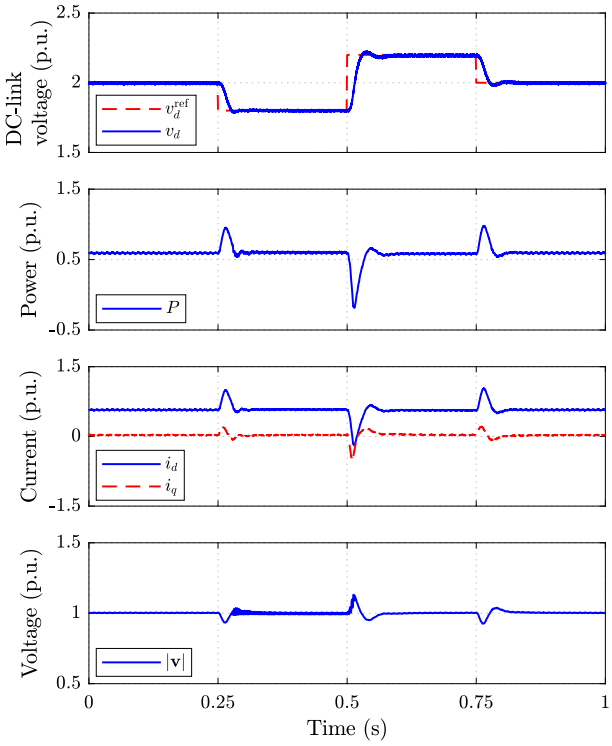

Fig. 16. Cascaded dc-link and active-power control for $\mathrm{SCR} = 3$.

$$\theta = \omega_1 t + \theta_0 + \Delta\theta \qquad \mathbf{i} = \mathbf{i}_0 + \Delta\mathbf{i} \tag{32}$$

where the load angle is confined to $-\pi/2 \leq \theta_0 \leq \pi/2$. This allows (1) to be transformed to the dq frame as

$$\mathbf{v} - [s + j\underbrace{(\omega_1 + \dot{\Delta\theta})}_{\dot{\theta}}]L\mathbf{i} = V_g e^{-j(\theta_0+\Delta\theta)}. \tag{33}$$

From (7), $\Delta\mathbf{v} = -H_a(s)\Delta\mathbf{i}$, which is substituted in (33). Approximating $e^{-j\Delta\theta} \approx 1 - j\Delta\theta$, and neglecting cross terms between perturbation variables yields, after simplification

$$\begin{aligned}[H_a(s) + (s + j\omega_1)L]\Delta\mathbf{i} =& j(V_g e^{-j\theta_0} - sL\mathbf{i}_0)\Delta\theta \\ &+ V - j\omega_1 L\mathbf{i}_0 - V_g e^{-j\theta_0}.\end{aligned} \tag{34}$$

The last three terms on the right-hand side of (34) must sum up to zero, i.e.,

$$V - j\omega_1 L\mathbf{i}_0 = V_g e^{-j\theta_0}. \tag{35}$$

Equation (34) now yields the following complex-transfer-function relation between $\Delta\theta$ and $\Delta\mathbf{i}$:

$$\Delta\mathbf{i} = \underbrace{\frac{j[V - (s + j\omega_1)L\mathbf{i}_0]}{H_a(s) + (s + j\omega_1)L}}_{\mathbf{G}_{\theta i}(s)}\Delta\theta \tag{36}$$

where (35) is used in the numerator. Introducing perturbation variables in (5) allows the active power to be expressed as

$$\begin{aligned}P &= \kappa\mathrm{Re}\{(V + \Delta\mathbf{v})(\mathbf{i}_0 + \Delta\mathbf{i})^*\} \\ &\approx \underbrace{\kappa\mathrm{Re}\{V\mathbf{i}_0^*\}}_{P_0} + \underbrace{\kappa\mathrm{Re}\{V\Delta\mathbf{i}^* + \mathbf{i}_0^*\Delta\mathbf{v}\}}_{\Delta P}\end{aligned} \tag{37}$$

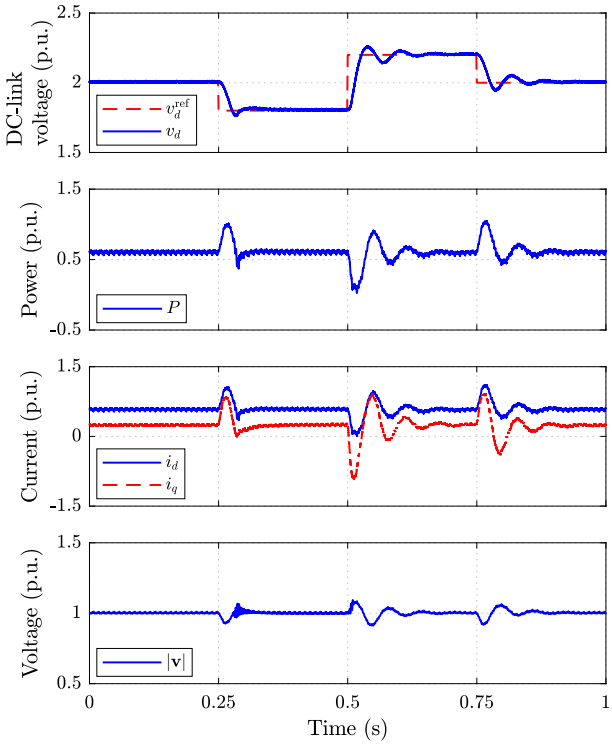

Fig. 17. Cascaded dc-link and active-power control for $\mathrm{SCR} = 10$.

where $\Delta\mathbf{v} = -H_a(s)\Delta\mathbf{i}$. Substitution of (36) in (37) then gives the desired relation between $\Delta\theta$ and ΔP

$$\Delta P = \underbrace{\kappa \mathrm{Re}\{V\mathbf{G}_{\theta i}^*(s) - H_a(s)\mathbf{i}_0^*\mathbf{G}_{\theta i}(s)\}}_{G_{\theta P}(s)}\Delta\theta \tag{38}$$

where the real part is evaluated for s real, giving (9).

Appendix II

Solving for ω in $\mathrm{Im}\{G_p(j\omega)\} = 0$ yields the phase crossover frequency $\omega_\pi = \sqrt{\omega_1^2 + (R_a/L)^2}$. The gain margin is found to be

$$\begin{aligned} g_m &= -\frac{1}{G_p(j\omega_\pi)} = \frac{2\omega_1 R_a}{\kappa K_p V^2}\frac{1+(\frac{R_a}{\omega_1 L})^2}{1+b-(\frac{R_a}{\omega_1 L})^2 a} \\ &= \frac{2\omega_1 R_a}{\kappa K_p V^2}\frac{1+(\frac{R_a}{\omega_1 L})^2}{1-(\frac{R_a|\mathbf{i}_0|}{V})^2}. \end{aligned} \tag{39}$$

Applying (13) yields

$$g_m = 2\underbrace{\frac{1+(\frac{R_a}{\omega_1 L})^2}{1-(\frac{R_a|\mathbf{i}_0|}{V})^2}}_{\geq 1} \geq 2. \tag{40}$$

Appendix III

Taking the real part of (35) gives $V + \omega_1 L i_{q0} = V_g \cos\theta_0$, which also can be expressed as

$$a = \frac{\omega_1 L i_{q0}}{V} = \frac{V_g}{V}\cos\theta_0 - 1. \tag{41}$$

Since the load angle is confined as $|\theta_0| \leq \pi/2$, $\cos\theta_0 \geq 0$, and consequently $a \geq -1$.

Appendix IV

Solving for ω in $\mathrm{Im}\{G_d(j\omega)\} = 0$ for $\omega_b = 0$ yields the phase crossover frequency $\omega_\pi = \sqrt{(1-b)/(2+a)}\omega_1$. The gain margin is found to be

$$g_m = -\frac{1}{G_d(j\omega_\pi)} = \frac{1}{K_d}\left[\frac{(1-b)\omega_1^2 L}{(2+a)R_a} + \frac{R_a}{2L}\right]. \tag{42}$$

The minimum value of (42) is obtained for $L = \sqrt{2}R_a/\omega_1$ and is given by

$$g_{m,\min} = \frac{\omega_1}{K_d}\sqrt{\frac{1-b}{2+a}}. \tag{43}$$

Hence, to get $g_m \geq 4$, (24) should be observed.

References

[1] H.-P. Beck and R. Hesse, "Virtual synchronous machine," in *Proc. 9th Int. Conf. Electr. Power Quality Util.*, Oct. 2007, pp. 1–6.

[2] L. Harnefors, "Control of a voltage source converter using synchronous machine emulation," International Patent WO 2010/022766, Mar. 2010.

[3] L. Zhang, L. Harnefors, and H.-P. Nee, "Power-synchronization control of grid-connected voltage-source converters," *IEEE Trans. Power Syst.*, vol. 25, no. 2, pp. 809–920, May 2010.

[4] Q. C. Zhong and G. Weiss, "Synchronverters: Inverters that mimic synchronous generators," *IEEE Trans. Ind. Electron.*, vol. 58, no. 4, pp. 1259–1267, Apr. 2011.

[5] L. Zhang, H.-P. Nee, and L. Harnefors, "Analysis of stability limitations of a VSC-HVDC link using power-synchronization control," *IEEE Trans. Power Syst.*, vol. 26, no. 3, pp. 1326–1337, Aug. 2011.

[6] Q. C. Zhong, P. L. Nguyen, Z. Ma, and W. Sheng, "Self-synchronized synchronverters: Inverters without a dedicated synchronization unit," *IEEE Trans. Power Electron.*, vol. 29, no. 2, pp. 617–630, Feb. 2014.

[7] M. Ashabani, F. D. Freijedo, S. Golestan, and J. M. Guerrero, "Inducverters: PLL-less converters with auto-synchronization and emulated inertia capability," *IEEE Trans. Smart Grid*, vol. 7, no. 3, pp. 1660–1674, May 2016.

[8] G. Wu, J. Liang, X. Zhou, Y. Li, A. Egea-Alvarez, G. Li, H. Peng, and X. Zhang, "Analysis and design of vector control for VSC-HVDC connected to weak grids," *CSEE J. Power Energy Syst.*, vol. 3, no. 2, pp. 115–124, Jun. 2017.

[9] L. Zhang, L. Harnefors, and H.-P. Nee, "Interconnection of two very weak ac systems by VSC-HVDC links using power-synchronization control," *IEEE Trans. Power Syst.*, vol. 26, no. 1, pp. 344–355, Feb. 2011.

[10] K. M. Alawasa and Y. A. R. I. Mohamed, "Impedance and damping characteristics of grid-connected VSCs with power synchronization control," *IEEE Trans. Power Syst.*, vol. 30, no. 2, pp. 952–961, Mar. 2015.

[11] A. A. A. Radwan and Y. A. R. I. Mohamed, "Power synchronization control for grid-connected current-source inverter-based photovoltaic systems," *IEEE Trans. Energy Conv.*, vol. 31, no. 3, pp. 1023–1036, Sep. 2016.

[12] S. I. Nanou and S. A. Papathanassiou, "Grid code compatibility of VSC-HVDC connected offshore wind turbines employing power synchronization control," *IEEE Trans. Power Syst.*, vol. 31, no. 6, pp. 5042–5050, Nov. 2016.

[13] Q. Fu, W. Du, C. Chen, H. F. Wang, and L. L. Fan, "Vector and power synchronization control for connecting a VSC-MTDC to an ac power system – A comparative study of dynamic interactions between the dc and ac network based on PSCAD simulation," in *Proc. 12 IET Int. Conf. AC DC Power Transm.*, May 2016, pp. 1–6.

[14] H. Wu, X. Ruan, D. Yang, X. Chen, W. Zhao, Z. Lv, Q. C. Zhong, "Small-signal modeling and parameters design for virtual synchronous generators," *IEEE Trans. Ind. Electron.*, vol. 64, no. 7, pp. 4292–4303, Jul. 2016.

[15] P. Mitra, L. Zhang, and L. Harnefors, "Offshore wind integration to a weak grid by VSC-HVDC links using power-synchronization control: A case study," *IEEE Trans. Power Del.*, vol. 29, no. 1, pp. 453–461, Feb. 2014.

[16] J. Liu, Y. Miura, and T. Ise, "Comparison of dynamic characteristics between virtual synchronous generator and droop control in inverter-based distributed generators," *IEEE Trans. Power Electron.*, vol. 31, no. 5, pp. 3600–3611, May 2016.

[17] R. H. Middleton and G. C. Goodwin, *Digital Control and Estimation – A Unified Approach*. Englewood Cliffs, NJ: Prentice Hall, 1994.
[18] Ö. Göksu, R. Teodorescu, C. L. Bak, F. Iov, and P. C. Kjaer, "Instability of wind turbine converters during current injection to low voltage grid faults and PLL frequency based stability solution," *IEEE Trans. Power Syst.*, vol. 29, no. 4, pp. 1683–1691, Jul. 2014.
[19] K. C. Divya and J. Østergaard, "Battery energy storage technology for power systems – An overview," *Electr. Power Syst. Res.*, vol. 79, no. 4, pp. 511–520, Apr. 2009.
[20] U. Manandhar, A. Ukil, G. H. Beng, N. R. Tummuru, S. K. Kollimalla, B. Wang, and K. Chaudhari, "Energy management and control for grid connected hybrid energy storage system under different operating modes," *IEEE Trans. Smart Grid*, early access, 2017.
[21] H. Bevrani, A. Ghosh, and G. Ledwich, "Renewable energy sources and frequency regulation: survey and new perspectives," *IET Renew. Power Gen.*, vol. 4, no. 5, pp. 438–457, Sep. 2010.
[22] O. Mo, S. D'Arco, and J. A. Suul, "Evaluation of virtual synchronous machines with dynamics or quasi-stationary machine models," *IEEE Trans. Ind. Electron.*, vol. 64, no. 7, pp. 5952–5962, Jul. 2017.
[23] M. P. N. van Wesenbeeck, S. W. H. de Haan, P. Varela, and K. Visscher, "Grid tied converter with virtual kinetic storage," in *Proc. IEEE Bucharest PowerTech*, Jun. 2009, pp. 1–7.
[24] W. Zhang, D. Remon, and P. Rodriguez, "Frequency support characteristics of grid-interactive power converters based on the synchronous power controller," *IET Renew. Power Gen.*, vol. 11, no. 4, pp. 470–479, 2017.
[25] M. Yu, A. J. Roscoe, C. D. Booth, A. Dyśko, R. Ierna, J. Zhu, and H. Urdal, "Use of an inertia-less virtual synchronous machine within future power networks with high penetrations of converters," in *Proc. 2016 Power Syst. Comput. Conf. (PSCC)*, Jun. 2016, pp. 1–7.

Lennart Harnefors (S'93–M'97–SM'07–F'17) received the M.Sc., Licentiate, and Ph.D. degrees in electrical engineering from the Royal Institute of Technology (KTH), Stockholm, Sweden, and the Docent (D.Sc.) degree in industrial automation from Lund University, Lund, Sweden, in 1993, 1995, 1997, and 2000, respectively. Between 1994–2005, he was with Mälardalen University, Västerås, Sweden, from 2001 as a Professor of electrical engineering. Between 2001–2005, he was, in addition, a part-time Visiting Professor of electrical drives with Chalmers University of Technology, Göteborg, Sweden. Since 2005, he has been with ABB, where he is currently a Senior Principal Scientist at Corporate Research, Västerås, Sweden. He is, in addition, a part-time Adjunct Professor of power electronics with KTH.

Dr. Harnefors is an Associate Editor of the IEEE TRANSACTIONS ON INDUSTRIAL ELECTRONICS. His research interests include control and dynamic analysis of power electronic systems, particularly grid-connected converters and ac drives.

Marko Hinkkanen (M'06–SM'13) received the M.Sc.(Eng.) and D.Sc.(Tech.) degrees in electrical engineering from the Helsinki University of Technology, Espoo, Finland, in 2000 and 2004, respectively.

He is an Associate Professor with the School of Electrical Engineering, Aalto University, Espoo. His research interests include control systems, electric drives, and power converters.

Dr. Hinkkanen was a General Co-Chair for the 2018 IEEE 9th International Symposium on Sensorless Control for Electrical Drives (SLED). He was the co-recipient of the 2016 International Conference on Electrical Machines (ICEM) Brian J. Chalmers Best Paper Award and the 2016 and 2018 IEEE Industry Applications Society Industrial Drives Committee Best Paper Awards. He is an Editorial Board Member of IET Electric Power Applications.

Usama Riaz received the B.E. degree in electrical engineering from the National University of Science and Technology (NUST), Islamabad, Pakistan, in 2015 and M.Sc.(Tech.) degree in automation and electrical engineering from Aalto University, Espoo, Finland, in 2018. He is currently working as a research assistant at the school of electrical engineering, Aalto University, Espoo, Finland.

His research interests include control of electric drives and grid converters, power systems, and renewable energy systems.

F. M. Mahafugur Rahman received the B.Sc.(Tech.) degree in electrical and electronic engineering from Chittagong University of Engineering and Technology, Chittagong, Bangladesh, in 2011. He received the M.Sc.(Tech.) degree in electronics and electrical engineering from Aalto University, Espoo, Finland, in 2016, where he is currently working towards the D.Sc.(Tech.) degree in electrical engineering.

His research interests include optimization and control of grid-connected converters.

Lidong Zhang (M'07–SM'11) was born in Shanxi province, China. He received the B.Sc. degree from the North China Electric Power University, Baoding, China, the Licentiate degree from Chalmers University of Technology, Göteborg, Sweden, and the Ph.D. degree from KTH Royal Institute of Technology, Stockholm, Sweden, in 1991, 1999, and 2010, respectively.

From 1991 to 1996, he worked as a Lecturer with the North China Electric Power University, Beijing, China. From 1999 to 2011, he worked as a System Engineer with ABB Power Systems, Ludvika, Sweden. Since 2012, he has been with the ABB Corporate Research, Västerås, Sweden, where he is currently a Principal Scientist. His research interests include HVDC, power system stability and control, and power quality. He is active in the Cigre working groups C4/C1/B4 and B4-57.